# Asymmetric Carbon Nanotube Dimers Embedded in a Dielectric Slab: New Plasmonic Resonance Behavior

SUMITRA DEY,[1,*] DEB CHATTERJEE,[1] EDWARD J. GARBOCZI,[2], AND AHMED M. HASSAN[1]

[1]*Department of Computer Science and Electrical Engineering, University of Missouri–Kansas City, Kansas City, MO 64110 USA*
[2]*Material Measurement Laboratory, Applied Chemicals and Materials Division, National Institute of Standards and Technology, Boulder, CO 80305 USA*
[*]*sumitra.dey@mail.umkc.edu*

**Abstract:** All prior work on modeling the full-wave electromagnetic response of carbon nanotubes (CNTs) have focused on CNTs in free-space, whereas in most practical applications, CNTs are embedded in a dielectric substrate. In this work, we use full-wave simulations to study the plasmonic resonances of CNT dimers embedded in a lossy dielectric slab with a finite thickness. The numerical results show that the finite thickness dielectric slab leads to the emergence of new CNT resonance behavior that is not present in a homogeneous environment. As a single CNT approaches the dielectric slab's interfaces, the resonance frequency of the CNT increases due to reduced dielectric loading. The resonance behavior changes completely when two CNTs in proximity form a dimer near the slab interface. The bonding and antibonding resonances of CNT dimers and the absorbed power vary significantly with the distance between the slab interface and the CNT dimer. Using this phenomenon, we show that symmetric CNT dimers can behave like asymmetric CNT dimers. Also, the antibonding resonance of an asymmetric CNT dimer can be suppressed by adjusting the length and depth of the CNT dimer inside the slab. This work can guide future sensing modalities based on CNT dimer as well as can provide an accurate assessment of the proximity of a CNT network to the interface of the embedding substrate.



## 1. Introduction

Carbon nanotubes (CNTs) are high-aspect ratio hollow pipe-like structures made of carbon atoms that exhibit length-dependent localized surface plasmon resonances (LSPR) in the terahertz (THz) through ultraviolet (UV) frequency range [1–4]. Advancement in sophisticated fabrication and nano-manipulation techniques made it possible to realize customized CNT configurations with high precision and scalability [5–8]. Concurrently, several efforts have been given to model the realistic shapes and complex spatial distribution of CNT networks accurately with full-wave electromagnetic solvers [9–11]. Many theoretical analyses have studied the electromagnetic properties of CNT networks commonly found in nanocomposite environments. These efforts can be broadly classified into two different approaches: (1) the dilute limit effective medium approximation (EMA) studies, such as the Waterman-Truell [12], and Maxwell-Garnett (MG) approximations [13, 14], and (2) full-wave electromagnetic analysis, such as using the method of moment (MoM), finite element method (FEM), or finite difference time domain method (FDTD) [9–11, 15–19]. Although the EMA approach provides simplified relations to evaluate the frequency dependent lossy dielectric properties of CNT composites, it suffers from multiple inconsistencies when compared to the experimental data [1, 20]. The EMA approach assumes low filler density and homogeneous environment, and thus it ignores the strong electromagnetic interactions among the CNTs and the interfaces of the embedding medium when in close

proximity. The results from the EMA can therefore be significantly different from the full-wave simulation results [11]. Recently with full-wave MoM modeling we have shown that the near electromagnetic field coupling between two CNTs in proximity create dual plasmonic resonances that are unique and depend on the configurational properties of the two CNT assembly, otherwise named as the CNT dimer [21]. This dual plasmon resonance phenomena can not be explained by the EMA models. Melnikov *et al.* has also pointed out the inconsistencies in the EMA approach while modeling the charge transport phenomena between two crossing CNTs in sub-nanometric vicinity [22].

Recent computational and experimental studies also show evidences of significant impact on the electromagnetic response of embedded CNTs due to the supporting dielectric medium. In an experimental study Long *et al.* showed that formation of a concentrated layer of CNTs near the composite surface enhance the surface conductivity of the CNT composite [23]. They used controlled UV exposure to selectively etch away the epoxy layer from the composite surface to reduce the distance between CNT rich micro-domains and the dielectric interface. Zhang *et al.* used FDTD simulation to show that adding ultrathin dielectric layer on top or below CNT based meta-material film can significantly red-shift the THz plasmon peaks and weaken the resonances [19]. In addition to the embedded condition, the response of CNTs are also found to vary when they are placed above a dielectric substrate as reported by Blancon *et al.* [24]. While measuring the extinction cross-section of an individual CNT supported on a silicon substrate, they observed noticeable broadening and red-shifts in CNT resonances, and modified relative peak amplitude as compared to the freely suspended CNT case [24].

The above studies indicate that the finite-thickness supporting substrate, which typically has a relative permittivity ($\varepsilon_r > 1$) and a loss tangent ($\tan(\delta) > 0$), significantly change the embedded CNT response. In this present paper we are particularly interested in studying the effect of finite thickness dielectric slab on the electromagnetic response of embedded two CNT network (CNT dimers) and asses its potential in sensing application. All previous computational studies related to two CNT networks have considered a homogeneous or free-space environment [21, 22]. The effect of a finite thickness embedding medium and its interaction with the embedded two CNT network has not yet been explored. In our previous work we have demonstrated the sensing modalities of CNT dimer in free-space environment using full-wave MoM simulations [21]. We explicitly demonstrated the near field coupling phenomena by introducing symmetry and asymmetry in CNT dimer assembly [21]. With respect to an incident plane wave excitation, the assembly of two CNT appears as a symmetric CNT dimer if both the CNTs are identical in every aspect, such as shape, size, alignment and chirality, otherwise it forms an asymmetric CNT dimer. It was observed that a length asymmetric CNT dimer illuminated by a plane wave excitation in free-space environment exhibits two plasmonic resonances: a bonding resonance (BR) and an antibonding resonance (ABR) [21]. The BR occurs when the currents in the two CNTs are in phase, whereas the ABR occurs when the currents in the two CNTs are out of phase. The BR typically appears at a higher frequency than the ABR. This dual plasmonic resonance phenomena has also been reported previously for other metallic nano-dimers involving structural asymmetries [25, 26]. In a recent study Gerislioglu *et al.* report that when the dielectric environment of gold dimers was modified a wide variety of additional resonances were observed [27].

In this paper our goal is to investigate how the BR and ABR of CNT dimer assembly respond to the change in its dielectric environment, especially when we transform homogeneous medium into finite thickness dielectric slab. We use our in-house full-wave MoM multilayer solver to account the effect of the finite thickness embedding medium and its interaction with the embedded CNT network [28, 29]. The in-house solver accurately solve the multiple reflections, transmissions, and absorption in the finite-thickness substrate and their effects on the embedded CNTs [28, 29]. Using this solver in our present study we demonstrate how the electromagnetic response of a

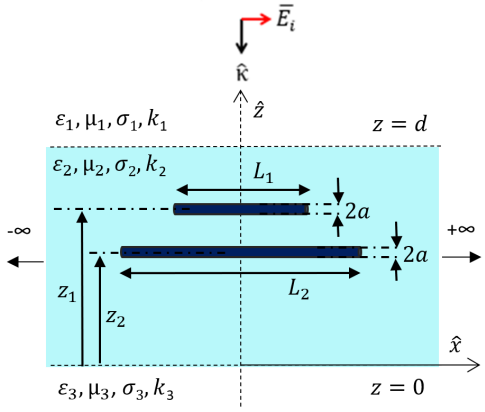


Fig. 1. Schematic diagram of a lossy three layer medium with an embedded CNT dimer in layer 2 illuminated by a plane wave polarized along the CNT length.

CNT dimer varies with the distance between the CNT dimer and the interface of the dielectric substrate, and create new plasmonic resonance modalities that are not observed when the CNTs are placed in a homogeneous dielectric environment.

## 2. Computational Model

Frequency domain full wave electromagnetic modeling of plasmonic structures requires highly dense mesh elements to accurately capture the nanoscale details especially when operating at THz or higher frequency range. Carbon based plasmonic materials, such as two dimensional graphene sheet, or three dimensional high aspect ratio carbon nanotubes face high volume discretization issues and unrealistic simulation time in conventional MoM or FEM solvers even when simulated in the free space environment. Recently alternative novel numerical approaches are proposed to minimize these discretization problems for plasmonic structures. For example, Shapoval *et al.* proposed 'meshless' algorithm based on the singular integral equations and Nystrom-type discretizations for simulating finite and infinite graphene strips in free space [30]. Hassan *et al.* proposed one dimensional equivalent arbitrary thin wire (ATW) model for high aspect ratio CNTs for free space MoM analysis and maintaining high solution accuracy [9, 21]. In addition to that, when high aspect ratio CNTs are embedded in layered medium their numerical modeling becomes a multiscale problem that increases the computational complexity by manifold. The conventional MoM and FEM models require thousands to millions of surface/volume discretization elements to accurately characterize the embedding dielectric layer as well as the embedded nanoscale tubes, and demand high computational time and resources as reported previously [11, 17]. Addressing these issues, we have recently developed an alternative MoM solver for studying electromagnetic scattering response of CNT composites that drastically reduce the discretization requirements and boost the computational speed by several hundred order over commercial MoM or FEM solvers while maintaining same level of accuracy [29]. The in-house solver uses the multilayer Green's function technique to avoid the explicit discretization of the embedding layer interfaces [31]. The embedded high-aspect ratio CNTs are modeled as arbitrary thin wires (ATW) that need only one-dimensional discretization [9, 21]. The accuracy and computational efficiency of this method are validated rigorously at multiple stages of development against commercial solvers [21, 28, 29]. In this article, we have used this in-house solver to study the CNT dimer embedded in a lossy dielectric layer.

Uncertainty in nanoscale fabrication may lead to many degrees of freedom in CNT dimer configuration, such as length asymmetry, shape anisotropy, misalignment etc. [21]. However,

to establish a proof of concept, in this paper we only investigate length asymmetry effect in non-collinear parallel CNT dimer embedded in a lossy dielectric slab as shown in Fig. 1. This study can easily be extended to other complicated CNT dimer configurations. The computational model considers a generic lossy three-layer structure where the CNTs are placed in layer 2 on the xz-plane symmetrically about their lengths and parallel to the dielectric interfaces with a fixed center to center distance of $|z_1 - z_2|$. The layered structure is illuminated by a plane wave ($\bar{E}^i$) incident normally on the top dielectric interface ($z = 0$). The CNTs are identical in every aspect except for their lengths. The CNTs have been assigned frequency dependent complex impedances derived from their Drude-like surface conductivity model similar to the previous works [21, 29]. This conductivity model agrees well with the quantum mechanical dynamic conductivity model for CNTs from the microwave through 100 THz frequency range, provided the CNTs are single-walled, metallic and have small radius (< 2 nm) [32]. In this present study, the CNTs are considered as single-walled with (9,9) armchair chirality that has a radius of $a$ = 0.61 nm [15]. The boundary condition that relates the total tangential electric field to the induced axial current on a CNT ($\bar{I}_{cnt}$) is given by:

$$\left[\bar{E}_2^i + \bar{E}_2^s\right]_{tan} = Z_{cnt}\,\bar{I}_{cnt} \tag{1}$$

where $\bar{E}_2^i$ is the incident electric field on CNT in layer 2, $\bar{E}_2^s$ is the scattered electric field from CNT in layer 2, and $Z_{cnt}$ is the frequency dependent complex impedance of a single walled CNT with (9,9) armchair chirality [29]. The absorption power ($P_{abs}$) of a one dimensional CNT of length $l$ in layer 2 can be evaluated at each operating frequency using [33],

$$P_{abs} = 0.5 \int_0^l |\bar{I}_{cnt}|^2\, \mathcal{R}e(Z_{cnt})\; dl \tag{2}$$

The strength of the illuminating plane wave incidenting normally on the top dielectric interface is set as $|\bar{E}^i|$ = 1 V/m for all computational experiments performed in this article. Thus the incident power density on the top dielectric interface is $\frac{|\bar{E}^i|^2}{\eta_0} = 2.65 \times 10^{-4}$ mW/cm$^2$, where $\eta_0 = 377\ \Omega$ is the free space wave impedance.

## 3. Computational Results and Discussion

### 3.1. Resonance of a Single CNT Embedded in a Finite Thickness Dielectric Slab

We start our analysis by investigating the effect of the height of a single CNT inside a finite thickness dielectric slab. Fig. 2(a) shows a schematic diagram of a horizontal CNT of length $L$ embedded in a lossy dielectric slab at a height $z_0$, and is illuminated by a plane wave polarized along the CNT length. The slab has a thickness $d$ = 50 nm, relative permittivity $\varepsilon_{r2}$ = 10, relative permeability $\mu_{r2}$ = 1, and conductivity $\sigma_2$ = 1 S/m. The slab is backed by air above/below the top/bottom interfaces. The present choice of slab properties are close to that of the silicon, one of the most commonly used substrate. However, the in-house solver can support a wide range of material properties ($\varepsilon_{ri}$ = 1 to 20, $\mu_{ri}$ = 1 to 20, $\sigma_i$ = 1 S/m to 20 S/m, for i=1,2,3), including 1 GHz to 10 THz operating frequency, nm to mm thick substrate, nm to cm range of lateral separation between source and observation point, to cover most CNT composite applications [29].

The absorbed power ($P_{abs}$) spectrum is calculated for two different CNT lengths ($L$ = 96 nm and $L$ = 86.4 nm) and with varying height of the CNT ($z_0 = 5, 15, 25, 35, 45$ nm) inside the slab. The CNT resonance frequencies inside the dielectric slab ($f_r$) are plotted in Fig. 2(b) showing a symmetric 'U' shape variation. The resonance frequency ($f_r$) for both CNT lengths reaches its minimum value when the CNT is placed at the middle of the dielectric slab ($z_0$ = 25 nm), and increases when approaching either of the top or bottom interface of the slab. This indicates that the embedded CNT experiences varying dielectric loading inside the slab which

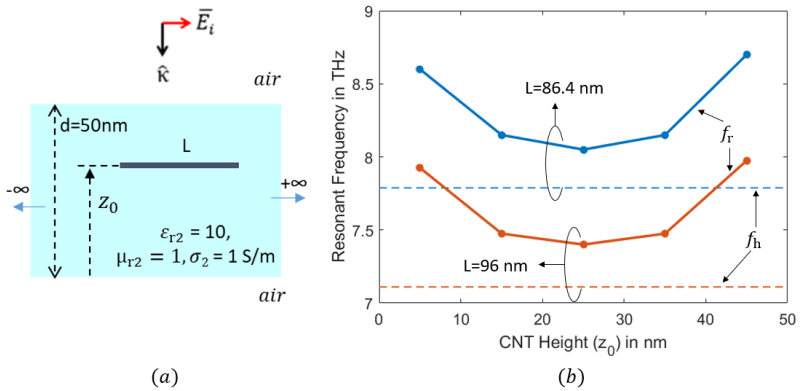


Fig. 2. (a) Schematic diagram of a horizontal CNT embedded in a finite thickness lossy dielectric slab at a particular height ($z_0$) illuminated by a plane wave polarized along the CNT length. (b) Variation of CNT resonance frequency with changing CNT height inside the dielectric slab ($f_r$), and comparison against CNT resonance in homogeneous medium ($f_h$) with same relative permittivity ($\varepsilon_r$ = 10).

is maximum at the middle of the slab and minimum near the slab-air interfaces. For better insight, we also calculate the CNT resonances while floating in a lossless homogeneous infinite medium with the same relative permittivity as the dielectric slab ($\varepsilon_r$ = 10) and is denoted by $f_h$. For the homogeneous case, the CNT resonance ($f_h$) remains constant and independent of $z_0$ as expected, since no interfaces are present. The 96 nm long CNT resonates at $f_h$ = 7.12 THz as depicted by the orange horizontal dashed line (Fig. 2(b)). The 86.4 nm long CNT resonates at $f_h$ = 7.79 THz as depicted by the blue horizontal dashed line (Fig. 2(b)). The CNT resonance inside the dielectric slab ($f_r$) is always slightly higher than the homogeneous case ($f_h$). This is because the CNT embedded in a finite thickness dielectric slab experiences less dielectric loading as compared to the homogeneous infinite medium of the same permittivity. To explain this phenomena quantitatively, we define the effective electrical length ($L'$) of a CNT under the influence of the dielectric slab using the following relation,

$$L' = L \times \frac{f_h}{f_r} \tag{3}$$

where $L$ is the physical length of the CNT, $f_h$ is the CNT resonance in homogeneous infinite medium with the same permittivity as the dielectric slab, and $f_r$ is the CNT resonance in the dielectric slab at a certain height $z_0$ (as in Fig. 2(a)). The effective electrical length $L'$ of a CNT at a particular height $z_0$ inside the slab can be thought of as the length of an otherwise identical CNT in a homogeneous, infinite medium, with the same dielectric constant as the slab, which has the same resonance frequency $f_r$. Since $f_r$ is always greater than $f_h$, the effective electrical length ($L'$) will always be less than the physical length of CNT ($L$). The CNT experiences maximum dielectric loading and longest effective electrical length at the middle of the slab. As the CNT moves closer to either of the slab interfaces the dielectric loading reduces, the effective CNT length decreases and thus the CNT resonates at higher frequency. If the slab thickness ($d$) becomes very large in comparison to the CNT length ($L$), then $f_r$ asymptotically approaches $f_h$. On the other hand, if the thickness of the slab drops to zero, the CNT is effectively placed in free-space and the 96 nm and 86.4 nm length CNTs will resonate at 23 THz and 25 THz respectively [21]. Therefore, embedding a CNT in a dielectric slab provides an intermediate resonance frequency to the case when the CNT is embedded in an infinite homogeneous dielectric medium and the case when the CNT is embedded in free-space.

### 3.2. Symmetric CNT Dimer Embedded in a Dielectric Slab vs in a Homogeneous medium

In this section we explain how a finite thickness slab can change the plasmonic resonance behavior of a length symmetric CNT dimer compared to its homogeneous medium response. We also show how the symmetry conditions are defined for embedded CNT dimer. We particularly focus on the longitudinal plasmon excitation (incident electric field being parallel to the CNT length) both in side-by-side and end-to-end dimer arrangements, inspired by the work of Jain *et al.* who studied plasmon coupling in gold nanorod assemblies in homogeneous medium [25].

Fig. 3(a) shows two CNTs at two different heights ($z_0$ = 45 nm, 33 nm) embedded in a dielectric slab. Both the CNTs have equal length of $L1 = L2 = 96$ nm and are placed in a non-collinear parallel arrangement where the incident electric field is aligned to the CNT lengths. Thus a length-symmetric side-by-side CNT dimer is formed with a 12 nm dimer gap. All other parameters remain the same as in Fig. 2(a). For ease of comparison, the choice of CNT length, dimer gap, and arrangement are intentionally kept similar to that of our previous work ( [21], Fig. 1), where we found that the non-collinear parallel CNT dimer with identical CNTs in free-space condition generate single plasmonic resonance which exhibits blue-shifts in frequency with decreasing dimer gap.

Presently, we compute the $P_{abs}$ for the symmetric CNT dimer of Fig. 3(a), i.e. when embedded in the dielectric slab as well as the case when the CNT dimer is placed in a lossless homogeneous space with $\varepsilon_r = 10$. Both $P_{abs}$ are plotted in Fig. 3(b). For the homogeneous case (blue curve) we see a single resonance at 7.9 THz denoted by $BR_h$ ($h$ stands for homogeneous medium) created by the in-phase currents flowing on both the CNTs typical of the bonding resonance. The anti-bonding resonance disappears as the equal magnitude out-of-phase currents cancel each other [21].

On the contrary, the same symmetric CNT dimer when embedded in the finite thickness dielectric slab produces two distinct resonances at 6.37 THz and at 8.86 THz (Fig. 3(b) orange curve). We plot the real and imaginary parts of the currents at these two frequencies flowing on the CNT dimer in Fig. 3(c) and 3(d), respectively. At 6.37 THz, the current is flowing out-of-phase on both CNTs (purple curve) creating an anti-bonding resonance (ABR). At 8.86 THz, the current is flowing in-phase on both CNTs (green curve) creating a bonding resonance (BR). It is interesting to observe that, although both the CNTs have equal physical length, the induced currents are unequal whether it is ABR or BR. At ABR, CNT 2 has a higher magnitude current than CNT 1. As a result, the out-of-phase current on both CNTs do not cancel each other completely and the ABR emerges at 6.37 THz. At BR, CNT 1 has a higher magnitude of current than CNT 2. This inequality in induced current is caused by the height dependent dielectric loading on the CNTs inside the slab. Being closer to the top interface (next to air), CNT 1 at $z_0$ = 45 nm experiences low dielectric loading and shorter effective electrical length than CNT 2 at $z_0$ = 33 nm. Thus, one significant contribution of this paper is to show that the differences in the relative height inside a slab is another mechanism that can break the symmetry in dimers, with identical CNTs, generating dual plasmon resonances.

We also observe in Fig. 3(c)-(d) that the bonding mode current is larger in magnitude than the anti-bonding mode current, which explains why BR has a much higher peak power than the ABR in Fig. 3(b). The BR for the embedded CNT dimer inside the dielectric slab is $\sim$ 12 % blue-shifted as compared to the homogeneous case ($BR_h$). Due to the reflection at the top interface and losses in the dielectric slab ($\sigma_2$ = 1 S/m), the peak absorbed power in the CNT dimer also decreases significantly ($\sim$ 19 dB) as compared to the lossless homogeneous case.

To confirm our hypothesis, we study a different kind of symmetric embedded CNT dimer as shown in Fig. 4(a), where the two CNTs are collinear as well as being parallel, commonly known as end-to-end dimer. All other parameters are same as in Fig. 3(a). Both the CNTs in Fig. 4(a) are placed at the same height $z_0$ = 45 nm with an end to end gap of 12 nm. We compute the $P_{abs}$

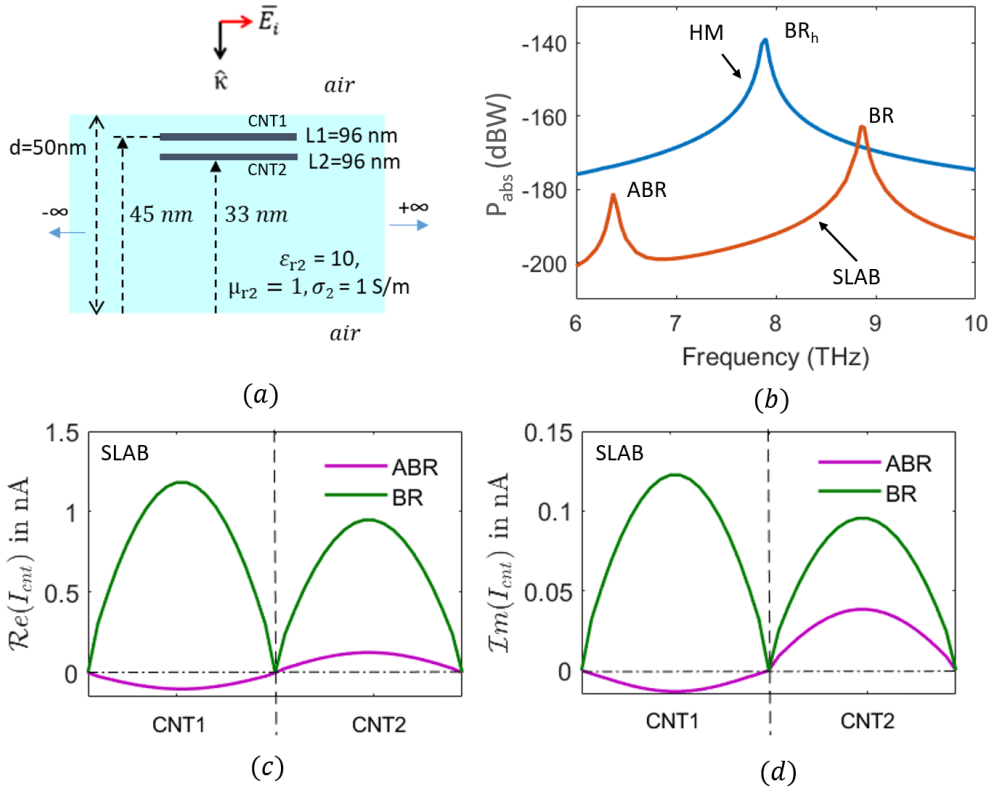


Fig. 3. (a) Schematic view of a symmetric CNT dimer embedded in a lossy dielectric slab. (b) Absorption power spectrum comparison of the symmetric CNT dimer embedded in the lossy dielectric slab (SLAB) Vs in a lossless homogeneous medium (HM) ($\varepsilon_r$ = 10). (c) Real and (d) imaginary part of the axial current ($I_{cnt}$) at anti-bonding resonance (ABR) and at bonding resonance (BR) flowing on the symmetric CNT dimer embedded in the dielectric slab.

for this end to end symmetric CNT dimer configuration when embedded in the dielectric slab as well as the case when the CNT dimer is placed in a lossless homogeneous infinite medium with $\varepsilon_r$ = 10, and both are plotted in Fig. 4(b). For the homogeneous case (blue curve) we only see a bonding resonance at 6.97 THz ($BR_h$) that follows a similar explanation as before in Fig. 3(b). In contrast to Fig. 3(b), the embedded CNT dimer of Fig. 4(b) (orange curve) exhibits only BR at 7.75 THz and no ABR. Since both the CNTs are placed at the same height inside the slab they experience the same dielectric loading and as a result have the same effective electrical length. Thus the equal magnitude out-of-phase current on both CNTs cancel each other completely and the ABR disappears. Fig. 4(c)-(d) show the real and imaginary components of the excited BR current of the embedded CNT dimer. The equal amplitude of BR current on both CNTs proves that they have equal effective electrical length when placed at the same height inside the slab. Thus using two identical CNTs it is possible to excite both ABR and BR (Fig. 3), or only BR (Fig. 4), just by varying the relative locations of embedded CNTs inside the slab.

### 3.3. *Asymmetric CNT Dimer in a Dielectric Slab*

In this section, we perform a comparative study between symmetric and asymmetric CNT dimers embedded in a dielectric slab with a finite thickness. Fig. 5 (top) shows three such embedded CNT dimer configurations: Case 1, Case 2, and Case 3. Case 1 is the same symmetric dimer

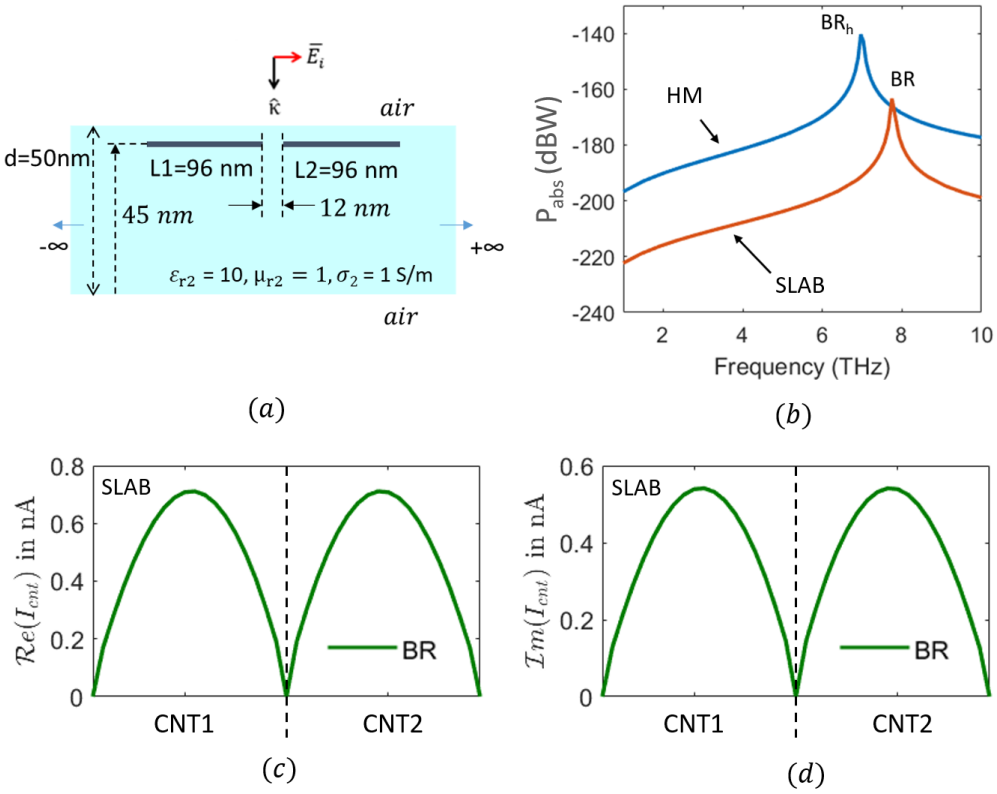


Fig. 4. (a) Schematic view of a symmetric end to end CNT dimer embedded in a lossy dielectric slab. (b) Absorption power spectrum comparison of the symmetric end to end CNT dimer embedded in the lossy dielectric slab (SLAB) Vs in a lossless homogeneous medium (HM) ($\varepsilon_r$ = 10). (c) Real and (d) imaginary part of the axial current ($I_{cnt}$) at the BR flowing on the symmetric CNT dimer embedded in the dielectric slab.

configuration with 96 nm long CNTs used in Fig. 3(a). Case 2 and Case 3 differ from Case 1 only by the CNTs' lengths. In Case 2, the top CNT is $L1$ = 96 nm long but the bottom CNT has a shorter physical length of $L2$ = 86.4 nm. Case 3 is the opposite of Case 2, where the top CNT has a shorter physical length of $L1$ = 86.4 nm and the bottom CNT is $L2$ = 96 nm long. In each case, the two CNTs are placed at two different heights ($z_0$ =45 nm, 33 nm) inside the slab such that the dimer separation is 12 nm. Fig. 5 (bottom) compares the computed $P_{abs}$ for all three cases. Both the ABR and BR show significant shifts in resonance frequency and peak power value among these three cases which is caused by the differences in dielectric loading on the embedded CNTs depending on their relative locations. To better explain the outcomes of Fig. 5 (bottom), we calculate the effective electrical lengths of the embedded CNTs used in Cases 1-3 for different heights using the relation (3) and are listed in Table 1. The equivalent CNT dimers with computed effective electrical lengths are shown in Fig. 5 in a dashed box just below the actual configurations. In all three cases, the effective electrical length of embedded CNT ($L'$) is smaller than their actual physical length ($L$). In Case 1, we see that $L'_1 < L'_2$. That means as a CNT moves towards the dielectric slab interface its effective electrical length decreases below its actual physical length. The symmetric dimer in Case 1, which has a zero difference in physical length ($\Delta L = L_1 - L_2 = 0$), while embedded in a dielectric slab behaves as a length asymmetric CNT dimer with a difference in effective electrical length $\Delta L' = L'_1 - L'_2 = 6$ nm. In Case 2, the asymmetric CNT dimer has a physical length difference of $\Delta L = 10$ nm, but the difference in effective electrical length is only $\Delta L' = 3$ nm. However, when we swapped the position of CNTs

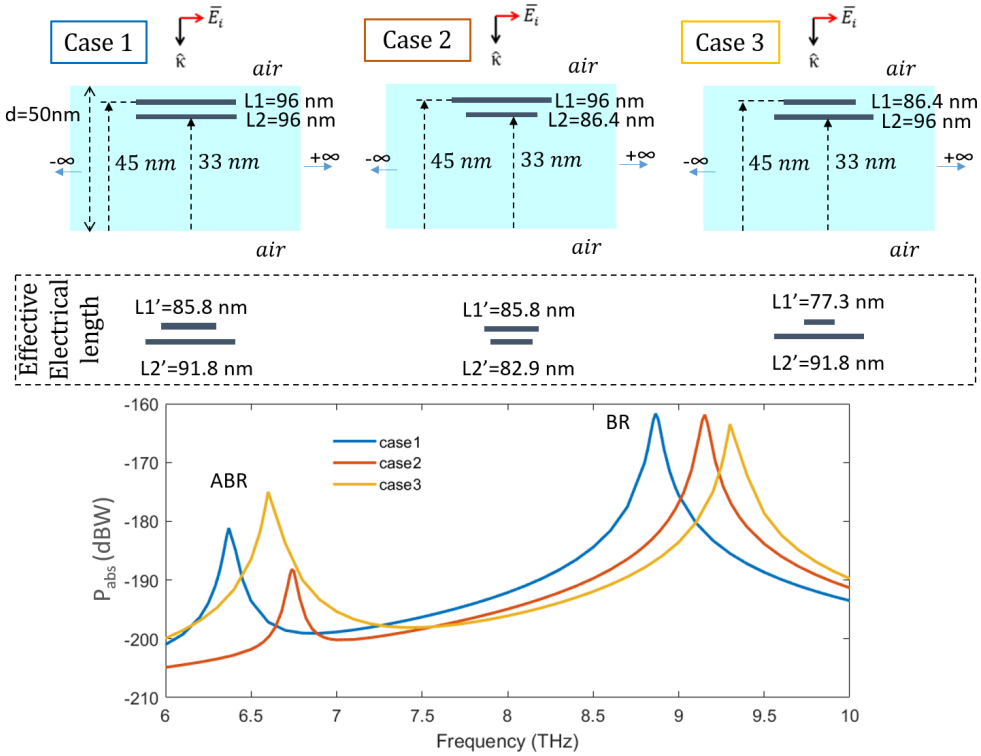


Fig. 5. (top) Case 1: symmetric embedded dimer; Case 2 and Case 3: asymmetric embedded dimer with swapped CNT position. (middle) Effective electrical lengths of the CNT dimers. (bottom) Absorption power comparison of the above three cases of embedded CNT dimers.

Table 1. Effective electrical length for embedded CNT

| CNT physical length (L) | CNT resonance in homogeneous space ($f_h$) | CNT height in slab ($z_0$) | CNT resonance in slab ($f_r$) | Effective electrical length $L' = L \times \frac{f_h}{f_r}$ |
|---|---|---|---|---|
| 96 nm | 7.12 THz | 45 nm | 7.97 THz | 85.8 nm |
| | | 33 nm | 7.45 THz | 91.8 nm |
| 86.4 nm | 7.79 THz | 45 nm | 8.7 THz | 77.3 nm |
| | | 33 nm | 8.12 THz | 82.9 nm |

from Case 2 to Case 3, we find a large difference in effective electrical length of $\Delta L' = 14.5$ nm. The power absorbed by a CNT ($P_{abs}$) at any frequency increases with the square of magnitude of the resulting current on the CNT dimer. At the ABR, the current increases with the difference in effective electrical lengths ($\Delta L'$) [21]. In Case 1, ($\Delta L' = 6$ nm), the peak $P_{abs}$ at the ABR is higher than that of Case 2 ($\Delta L' = 3$ nm) and lower than that of Case 3 ($\Delta L' = 14.5$ nm). On the contrary, the peak $P_{abs}$ at the BR increases with the sum of effective electrical lengths of the dimer ($\sum L' = L'_1 + L'_2$). For Case 1, $\sum L' = 177.6$ nm, for Case 2 and Case 3 they are close to $\sum L' = 169$ nm. If the asymmetric CNT dimers of Case 2 and Case 3 are placed in a lossless homogeneous space with $\varepsilon_r = 10$, an identical $P_{abs}$ will be achieved as expected. In spite of the swapped CNT position, no differences in resonance frequency or in peak power level will be

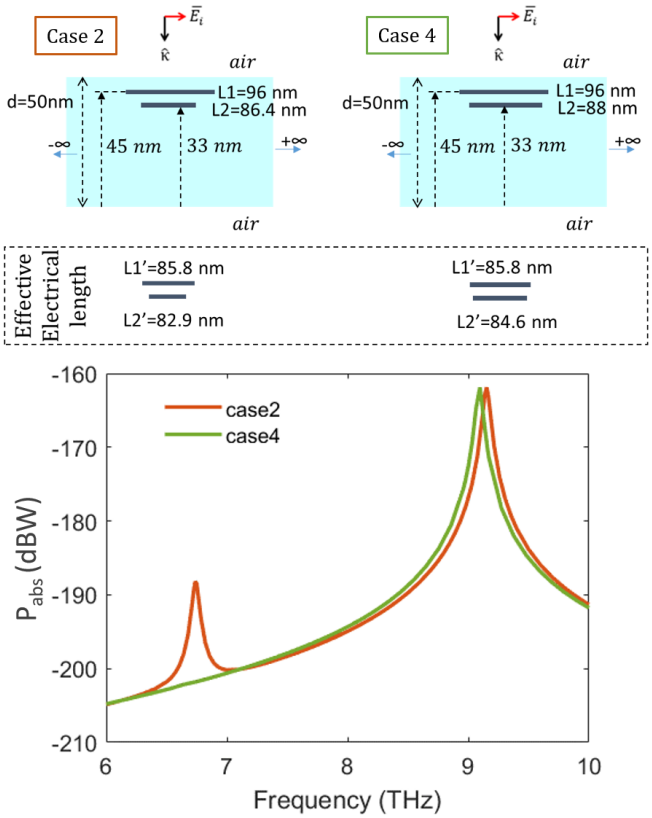


Fig. 6. Finding a special case of embedded asymmetric CNT dimer which eliminates its ABR from the absorption power spectrum. (top) Starting from the asymmetric CNT dimer of Case 2, the length of CNT 2 ($L_2$) is increased in finer steps to achieve Case 4 which shows no ABR. (middle) Effective electrical lengths of CNTs in embedded condition. For Case 2 $\Delta L' \approx 3$ nm and for Case 4 $\Delta L' \approx 1$ nm.(bottom) Absorption power spectrum for Case 2, which shows ABR and BR, and for Case 4, which shows only BR and no ABR.

seen between Case 2 and Case 3 in the infinite homogeneous medium. Hence, it is clear that the shift in resonance and power level found in Fig. 5 is due to the presence of the finite thickness dielectric slab.

### *3.4. Canceling the ABR in an Asymmetric CNT Dimer Embedded in a Dielectric Slab*

In Fig. 5, we showed that Case 2 ($\Delta L' = 3$ nm) had the minimum $P_{abs}$ at the ABR among all three cases. The ABR vanishes when the two CNTs in the dimer are approximately symmetric. However, the contribution of this section is to highlight that the symmetry for CNTs embedded in a dielectric slab with a finite thickness has to be in the effective length and not the physical length. To realize an equivalent symmetric CNT dimer embedded in a dielectric slab we need $\Delta L' \rightarrow 0$. In Case 2, $\Delta L'$ can be reduced either by decreasing $L_1'$ or by increasing $L_2'$. This can be achieved either by tuning the CNT physical length ($L$) or its height ($z_0$). In Fig. 6 (top), Case 4 shows one such tuned CNT dimer derived from Case 2. Keeping all other parametric values constant, the value of $L_2$ was increased from 86.4 nm, in fine steps until $L_2 = 88$ nm, at which the ABR disappears from the $P_{abs}$ spectrum as shown in Fig. 6 (bottom) green curve. The resultant difference in effective electrical length is found to be only $\Delta L' \approx 1$ nm (Fig. 6 (middle)), which agrees with our hypothesis.

## 4. Conclusion and Future Work

This study shows that carbon nanotubes (CNTs) embedded in a finite thickness dielectric slab exhibit new plasmon resonance phenomena that cannot be explained by the homogeneous medium model. The electromagnetic scattering response and the resonance change with the relative distance between the embedded CNTs and the interfaces of the dielectric slab. As the CNTs move towards the slab interface, their effective electrical length decreases causing a blue-shift in their resonance frequency. By optimizing the CNTs' lengths, distribution, and their proximity to the slab interfaces, it is possible to control their resonance frequencies and absorption power. Therefore, physically symmetric CNT dimers can behave like asymmetric CNTs when embedded in a dielectric slab. The shift in the bonding resonance (BR) and the anti-bonding resonance (ABR), and the variation in peak power level under the influence of the embedding layer can be very useful in developing CNT dimer based nano-sensing applications. For example, a new sensing modality could be realized by monitoring the ABR and designing the lengths and height separation of the CNTs in the dimer such that the ABR only vanishes when a dielectric with a specific permittivity and thickness is present. In practical applications, the fabricated CNTs are mostly skewed and it is difficult to align them perfectly. Thus any potential sensitivity issues arising from non-uniformity of embedded CNTs should be investigated in details while developing CNT dimer based sensors. In nano-composite environment CNTs try to aggregate and thus the spectrum will be splitting into more and more resonances, culminating in a band for a CNT film. In such scenario, the computational model presented herein can be useful in evaluating the proximity of CNTs to the interface of the composite in the THz non-destructive evaluation. Thus our future work will extend the present analysis to more complex embedded CNT distribution, including the sensitivity towards diverse orientations, alignments, and inter-tube proximity.

**Funding.** This work was supported in part by the NIST grant # 70NANB15H285 titled "Multi-Scale Computational Modeling of Carbon Nanostructure Composites" and in part by NSF CRI Award # 1629908 "II-NEW: Experimental Characterization and CAD Development Testbed for Nanoscale Integrated Circuits."

## References

1. P. Karlsen, M. V. Shuba, C. Beckerleg, D. I. Yuko, P. P. Kuzhir, S. A. Maksimenko, V. Ksenevich, H. Viet, A. G. Nasibulin, R. Tenne, and E. Hendry, "Influence of nanotube length and density on the plasmonic terahertz response of single-walled carbon nanotubes," J. Phys. D: Appl. Phys. **51**, 014003 (2017).
2. Q. Zhang, E. H. Hároz, Z. Jin, L. Ren, X. Wang, R. S. Arvidson, A. Lüttge, and J. Kono, "Plasmonic nature of the terahertz conductivity peak in single-wall carbon nanotubes," Nano Lett. **13**, 5991–5996 (2013).
3. Y. Wang, Z. Cui, D. Zhu, X. Zhang, and L. Qian, "Tailoring terahertz surface plasmon wave through free-standing multi-walled carbon nanotubes metasurface," Opt. Express **26**, 15343–15352 (2018).
4. F. Wang, M. Y. Sfeir, L. Huang, X. M. H. Huang, Y. Wu, J. Kim, J. Hone, S. O'Brien, L. E. Brus, and T. F. Heinz, "Interactions between individual carbon nanotubes studied by rayleigh scattering spectroscopy," Phys. Rev. Lett. **96**, 167401 (2006).
5. C. Thelander and L. Samuelson, "AFM manipulation of carbon nanotubes: realization of ultra-fine nanoelectrodes," Nanotechnology **13**, 108–113 (2002).
6. S. Heeg, N. Clark, and A. Vijayaraghavan, "Probing hotspots of plasmon-enhanced raman scattering by nanomanipulation of carbon nanotubes," Nanotechnology **29**, 465710 (2018).
7. T. Hertel, R. Martel, and P. Avouris, "Manipulation of individual carbon nanotubes and their interaction with surfaces," The J. Phys. Chem. B **102**, 910–915 (1998).
8. W. Xu, D. Ravichandran, S. Jambhulkar, Y. Zhu, and K. Song, "Hierarchically structured composite fibers for real nanoscale manipulation of carbon nanotubes," Adv. Funct. Mater. **31**, 2009311 (2021).
9. A. M. Hassan, F. Vargas-Lara, J. F. Douglas, and E. J. Garboczi, "Electromagnetic resonances of individual single-walled carbon nanotubes with realistic shapes: A characteristic modes approach," IEEE Transactions on Antennas Propag. **64**, 2743–2757 (2016).
10. A. M. Hassan, F. Vargas-Lara, J. F. Douglas, and E. J. Garboczi, "Electromagnetic scattering from multiple single-walled carbon nanotubes having tumbleweed configurations," IEEE Transactions on Antennas Propag. **65**, 3192–3202 (2017).
11. A. M. Hassan, M. K. Islam, S. On, B. Natarajan, I. Y. Stein, N. Lachman, E. Cohen, B. L. Wardle, R. Sharma, J. A. Liddle, and E. J. Garboczi, "Modeling the electromagnetic scattering characteristics of carbon nanotube composites

characterized by 3-d tomographic transmission electron microscopy," IEEE Open J. Antennas Propag. **1**, 142–158 (2020).
12. M. V. Shuba, A. V. Melnikov, A. G. Paddubskaya, P. P. Kuzhir, S. A. Maksimenko, and C. Thomsen, "Role of finite-size effects in the microwave and subterahertz electromagnetic response of a multiwall carbon-nanotube-based composite: Theory and interpretation of experiments," Phys. Rev. B **88**, 045436 (2013).
13. Z. Dang, J. Yuan, J. Zha, T. Zhou, S. Li, and G. hua Hu, "Fundamentals, processes and applications of high-permittivity polymer–matrix composites," Prog. Mater. Sci. **57**, 660–723 (2012).
14. E. Dadrasnia, S. Puthukodan, and H. Lamela, "Terahertz electrical conductivity and optical characterization of composite nonaligned single- and multiwalled carbon nanotubes," J. Nanophotonics **8**, 1 – 11 (2014).
15. G. W. Hanson, "Fundamental transmitting properties of carbon nanotube antennas," IEEE Transactions on Antennas Propag. **53**, 3426–3435 (2005).
16. J. Hao and G. W. Hanson, "Electromagnetic scattering from finite-length metallic carbon nanotubes in the lower ir bands," Phys. Rev. B **74**, 035119 (2006).
17. Y. Wang, S. Kim, G. Li, and L. Sun, "Filler orientation effect on relative permittivity of dielectric elastomer nanocomposites filled with carbon nanotubes," Comput. Mater. Sci. **104**, 69–75 (2015).
18. H. Lin, M. F. Pantoja, S. G. Garcia, A. R. Bretones, and R. G. Martin, "An fdtd thin-wire model for modeling carbon nanotube dipoles at thz regime," IEEE Antennas Wirel. Propag. Lett. **11**, 708–711 (2012).
19. X. Zhang, Y. Wang, Z. Cui, X. Zhang, S. Chen, K. Zhang, and X. Wang, "Carbon nanotube-based flexible metamaterials for thz sensing," Opt. Mater. Express **11**, 1470–1483 (2021).
20. M. V. Shuba, A. G. Paddubskaya, P. P. Kuzhir, S. A. Maksimenko, E. Flahaut, V. Fierro, A. Celzard, and G. Valusis, "Short-length carbon nanotubes as building blocks for high dielectric constant materials in the terahertz range," J. Phys. D: Appl. Phys. **50**, 08LT01 (2017).
21. S. Dey, E. J. Garboczi, and A. M. Hassan, "Electromagnetic resonance analysis of asymmetric carbon nanotube dimers for sensing applications," Nanotechnology **31**, 425501 (2020).
22. A. V. Melnikov, P. P. Kuzhir, S. A. Maksimenko, G. Y. Slepyan, A. Boag, O. Pulci, I. A. Shelykh, and M. V. Shuba, "Scattering of electromagnetic waves by two crossing metallic single-walled carbon nanotubes of finite length," Phys. Rev. B **103**, 075438 (2021).
23. C. J. Long, N. D. Orloff, K. A. Twedt, T. Lam, F. Vargas-Lara, M. Zhao, B. Natarajan, K. C. Scott, E. Marksz, T. Nguyen, J. F. Douglas, J. McClelland, E. Garboczi, J. Obrzut, and J. A. Liddle, "Giant surface conductivity enhancement in a carbon nanotube composite by ultraviolet light exposure," ACS Appl. Mater. & Interfaces **8**, 23230–23235 (2016).
24. J.-C. Blancon, M. Paillet, H. N. Tran, X. T. Than, S. A. Guebrou, A. Ayari, A. S. Miguel, N.-M. Phan, A.-A. Zahab, J.-L. Sauvajol, N. D. Fatti, and F. Vallée, "Direct measurement of the absolute absorption spectrum of individual semiconducting single-wall carbon nanotubes," Nat. Commun. **4**, 2542 (2013).
25. P. K. Jain, S. Eustis, and M. A. El-Sayed, "Plasmon coupling in nanorod assemblies: optical absorption, discrete dipole approximation simulation, and exciton-coupling model," The J. Phys. Chem. B **110**, 18243–18253 (2006).
26. T.-S. Deng, J. Parker, Y. Yifat, N. Shepherd, and N. F. Scherer, "Dark plasmon modes in symmetric gold nanoparticle dimers illuminated by focused cylindrical vector beams," The J. Phys. Chem. C **122**, 27662–27672 (2018).
27. B. Gerislioglu, L. Dong, A. Ahmadivand, H. Hu, P. Nordlander, and N. J. Halas, "Monolithic metal dimer-on-film structure: New plasmonic properties introduced by the underlying metal," Nano Lett. **20**, 2087–2093 (2020).
28. S. Dey, D. Chatterjee, E. J. Garboczi, and A. M. Hassan, "Novel electromagnetic scattering model for carbon nanotube composites using the multilayer green's function approach," in *2019 IEEE International Symposium on Antennas and Propagation and USNC-URSI Radio Science Meeting,* (2019), pp. 1297–1298.
29. S. Dey, D. Chatterjee, E. Garboczi, and A. M. Hassan, "Method of moment analysis of carbon nanotubes embedded in a lossy dielectric slab using a multilayer dyadic green's function," TechRxiv. [Preprint] (2021).
30. O. V. Shapoval, J. S. Gomez-Diaz, J. Perruisseau-Carrier, J. R. Mosig, and A. I. Nosich, "Integral equation analysis of plane wave scattering by coplanar graphene-strip gratings in the thz range," IEEE Transactions on Terahertz Sci. Technol. **3**, 666–674 (2013).
31. C. Tai, *Dyadic Green Functions in Electromagnetic Theory* (United Kingdom : IEEE Press, 1994).
32. A. M. Nemilentsau, "Tutorial: Linear surface conductivity of an achiral single-wall carbon nanotube," J. Nanophotonics **5**, 1 – 8 (2011).
33. A. G. Polimeridis, M. T. H. Reid, S. G. Johnson, J. K. White, and A. W. Rodriguez, "On the computation of power in volume integral equation formulations," IEEE Transactions on Antennas Propag. **63**, 611–620 (2015).